Electronic Supplementary Information

Silver nanoparticles embedded polymer-zirconium-based metal–organic framework (polyUiO-66) for electrochemical biosensors of respiratory viruses

Qiaojuan Jia, Yafei Lou, Feilong Rong, Shuai Zhang, Minghua Wang, Linghao He, Zhihong Zhang* and Miao Du*

College of Material and Chemical Engineering, Zhengzhou University of Light Industry, Zhengzhou 450001, P. R. China

* Corresponding authors.

E-mail address: mainzhh@163.com (Z. Zhang) and dumiao@zzuli.edu.cn (M. Du)

Content

S1. Experimental section

S1.1 Reagents and materials

All chemicals were of analytical reagent grade and used without purification. 2,5-Dihydroxyterephthalic acid, methanol, ethanol, dichloromethane, 1,8-dibromooctane, HCl, tetrahydrofuran, NaOH, and $NaHCO_3$ were purchased from Aladdin Reagent Co. Ltd. (Shanghai, China). Influenza A and B (Flu-A and Flu-B), mycoplasma pneumoniae (PI), chlamydia pneumoniae (CPN), and human serum were purchased from Solarbio Bioengineering Ltd. (Beijing, China). KH_2PO_4, $Na_2HPO_4 \cdot 12H_2O$, $K_3[Fe(CN)_6]$, KCl, NaCl, and $K_4[Fe(CN)_6] \cdot H_2O$ were purchased from Sinopharm Chemical Reagent Co. Ltd. (Beijing, China). All solutions were prepared with Milli-Q ultrapure water.

S1.2 Synthesis

The polymer ligand was synthetized by the reported procedure (*Angew. Chem. Int. Ed.*, **2015**, *54*, 6152) and characterized by ^{1}H NMR [(^{1}H-NMR, 400 MHz, DMSO-d_6), δ 7.25 (s, 2H), 3.99 (t, J = 8.0 Hz, 4H), 1.68 (t, J = 8.0 Hz, 4H), 1.42-1.32 (m, 8H)] (**Fig. S1**). UiO-66 was also prepared according to the reference procedure (*J. Am. Chem. Soc.*, **2008**, *130*, 13850).
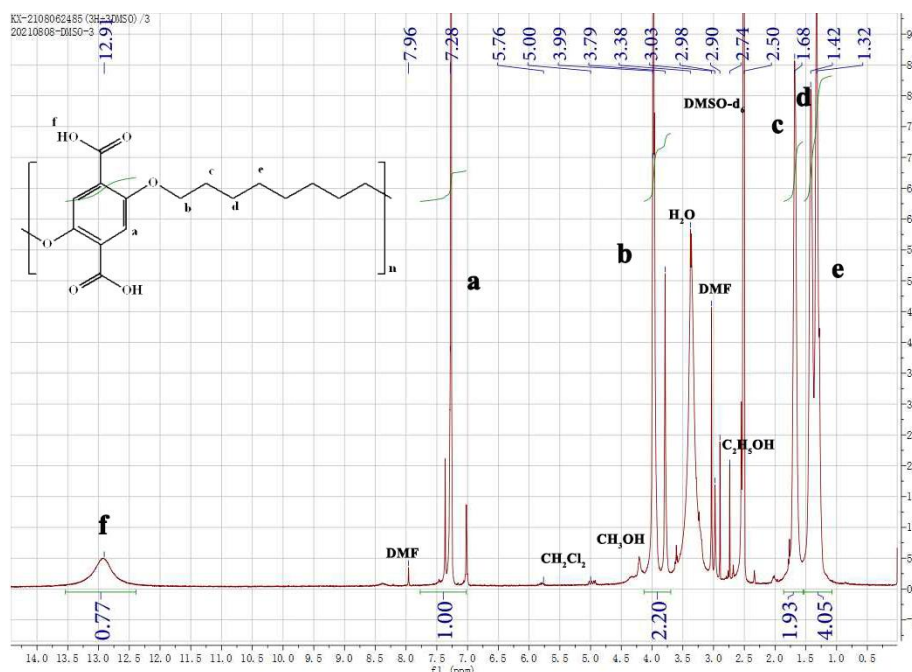

Fig. S1 ^{1}H-NMR spectrum of the polymer ligand.

S1.3 Preparation of solutions

Phosphate buffered saline (PBS, 0.1 M, pH = 7.4) was prepared by mixing 0.242 g KH_2PO_4, 1.445 g $Na_2HPO_4 \cdot 12H_2O$, 0.200 g KCl, and 8.003 g NaCl in water. And the electrolyte was prepared by dissolving 1.65 g $K_3Fe(CN)_6$ and 2.111 g $K_4Fe(CN)_6$ into 1 L of PBS.

S1.4 Characterizations

Powder X-ray diffraction (PXRD) was conducted using a Rigaku D/Max-2500 X-ray diffractometer with Cu Kα radiation (λ = 0.15406 nm). Fourier transform infrared (FT-IR) spectroscopy was taken by using a Bruker TENSOR 27 spectrometer (32 scans at 4 cm^{-1} resolution). X-ray photoelectron spectroscopy (XPS) was performed using an ESCALAB 250Xi spectrometer (Thermo Fisher Scientific, Manchester, UK) with Al Kα X-ray source (1486.6 eV photons). The surface morphology was studied on a JEOL JSM-6490LV field emission scanning electron microscope (FE-SEM, Japan) and JEOL JEM-2100 high-resolution transmission electron microscopy (HR-TEM, Japan) with a field emission gun of 200 kV. The statistics of particle size was taken using the ImageJ software.

S1.5 Pretreatment of Au electrode

The Au electrode (AE) with 3 mm diameter was treated prior to use. The AE was polished with 0.05 µm alumina slurry and then sonicated in piranha solution (v/v = 3/1 H_2SO_4/H_2O_2), ethanol, and water for 15 min, respectively. Afterwards, the Au electrode was activated via performing the cyclic voltammetry at a potential range of -0.2 V and +1.6 V in a solution containing 0.5 M H_2SO_4.

S1.6 EIS spectra and the equivalent circuit

The electrochemical impedance spectra (EIS) were analyzed by ZView2 software, in which the charge transfer resistance (R_{ct}) of electrode at each step can be represented by the amount of probes. The impedance spectra contain a semicircle and linear portion (**Fig. S2**). The semicircle portion at high frequencies corresponds to electron-transfer

limited process, and the linear portion at low frequencies represents diffusion process, where the semicircle diameter equals to electron transfer resistance (R_{ct}). A nonlinear least-squares fitting was used to determine the parameters in the equivalent circuit (**Fig. S2** inset), including solution resistance (R_s), charge-transfer resistance (R_{ct}), constant-phase element (CPE), and Warburg impedance (W).
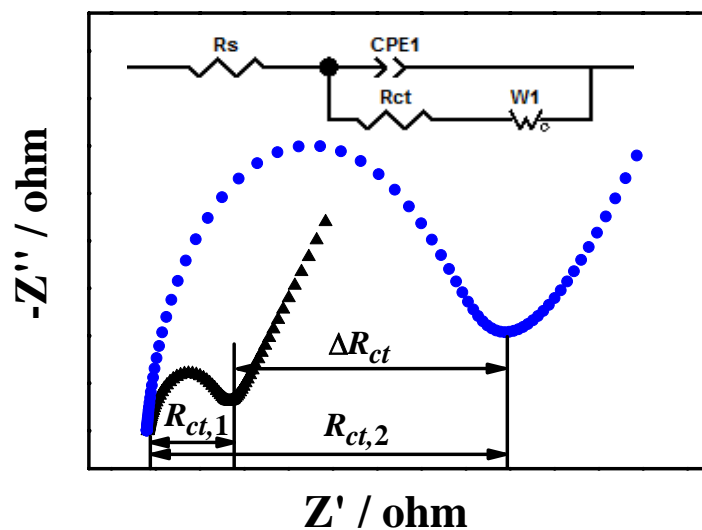

Fig. S2 EIS Nyquist plot (inset: the equivalent circuit).

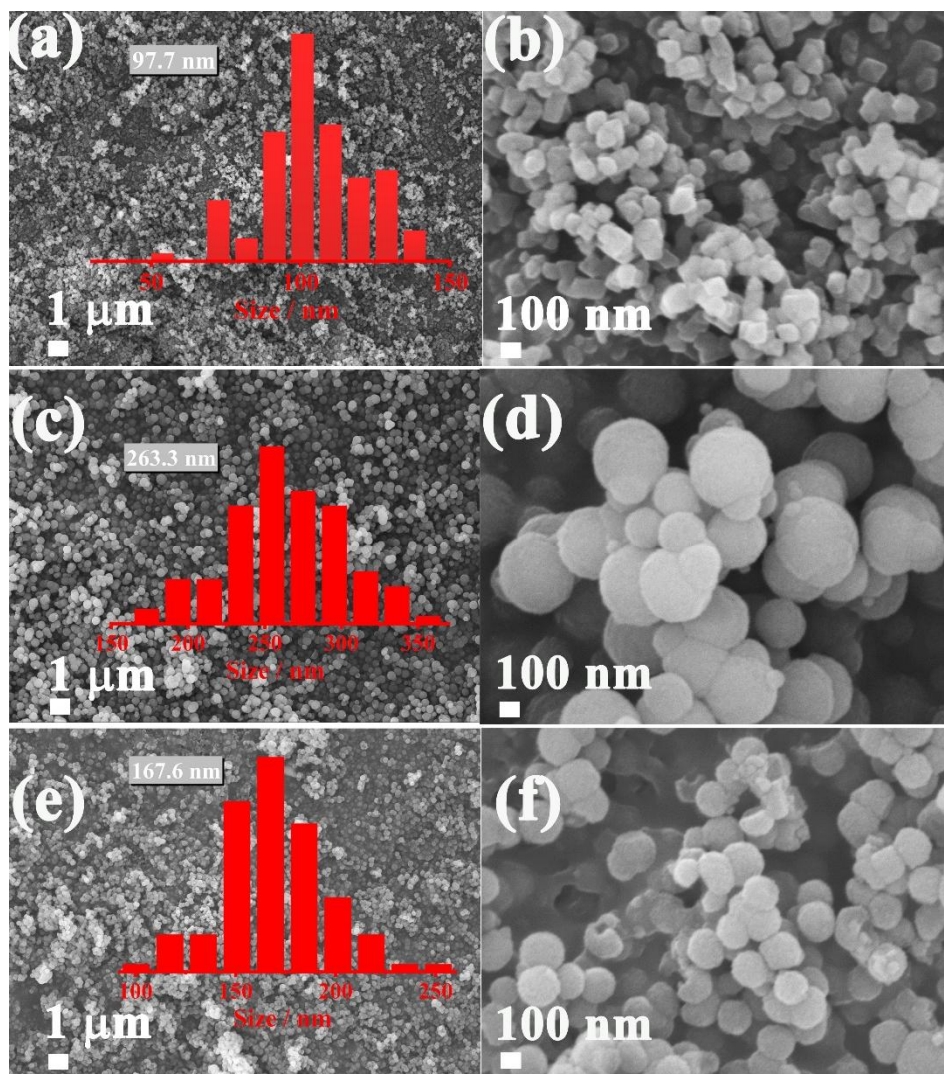**S2. Characterizations of UiO-66, polyUiO-66, and polyUiO-66@AgNPs**

Fig. S3 Low- and high-magnification SEM images of (a, b) UiO-66, (c, d) polyUiO-66, and (e, f) polyUiO-66@AgNPs.
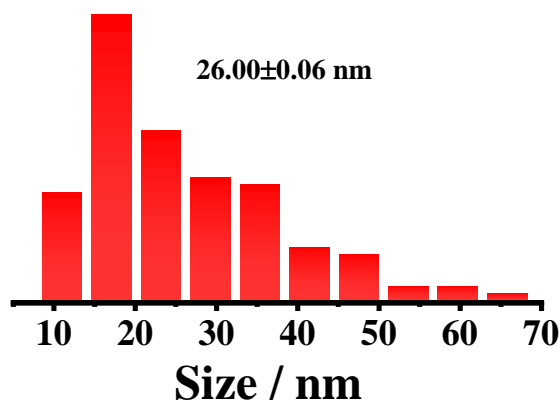
Fig. S4 Particle size distribution of AgNPs calculated from the TEM images of polyUiO-66@AgNPs.
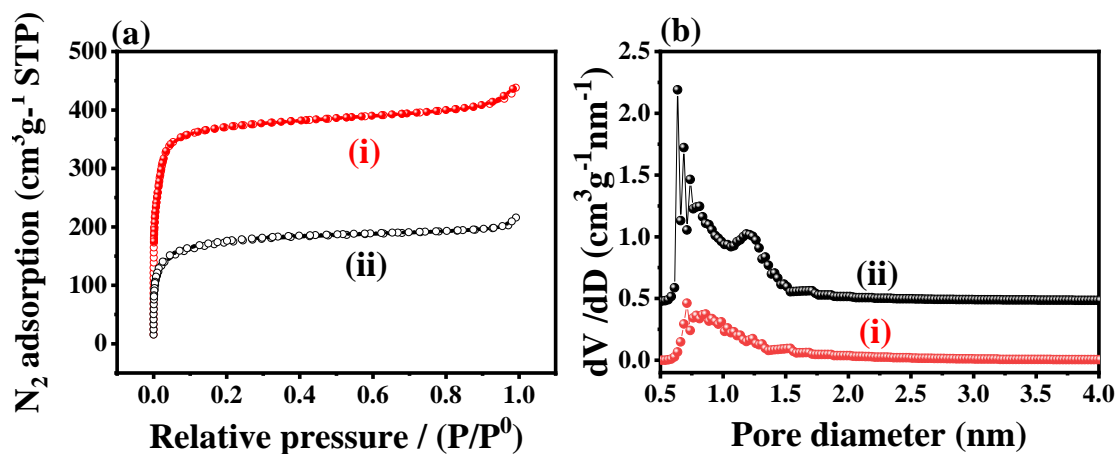
Fig. S5 (a) Nitrogen adsorption-desorption isotherm and (b) HK pore size distribution of (i) UiO-66 and (ii) UiO-66@AgNPs.
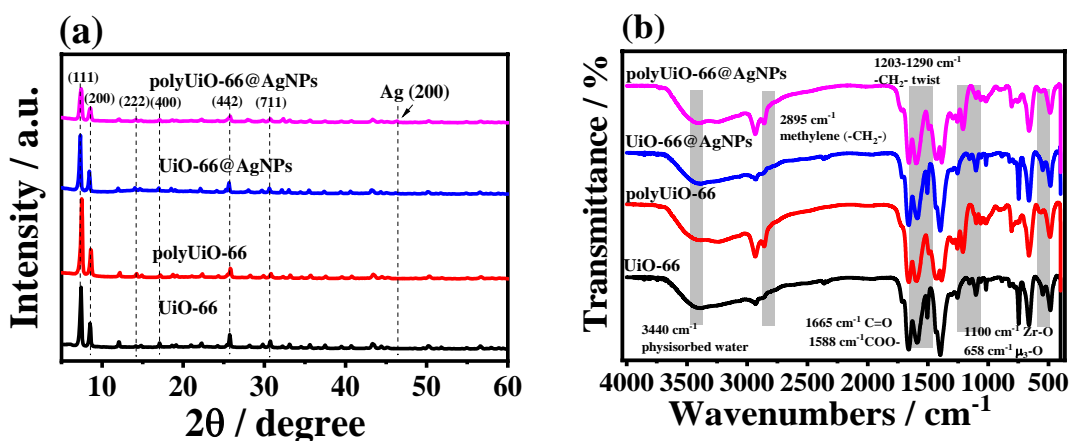
Fig. S6 (a) PXRD patterns and (b) FT-IR spectra of UiO-66, polyUiO-66, UiO-66@AgNPs and polyUiO-66@Ag NPs.
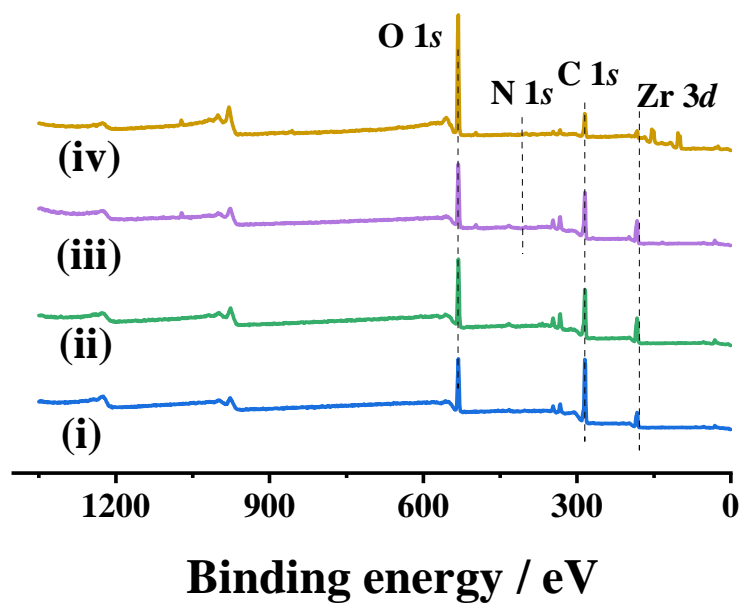
Fig. S7 XPS survey scan spectra of (i) polyUiO-66, (ii) polyUiO-66@AgNPs, (iii) Apt/polyUiO-66@Ag NPs, and (iv) Ab/polyUiO-66@AgNPs.
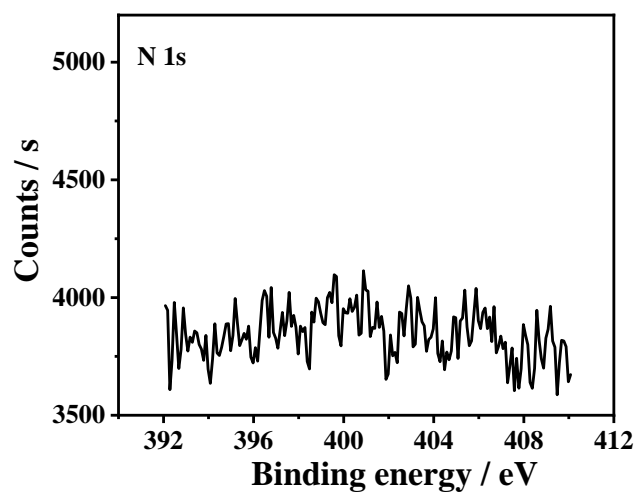
Fig. S8 High-resolution N 1*s* XPS spectrum of polyUiO-66@AgNPs.
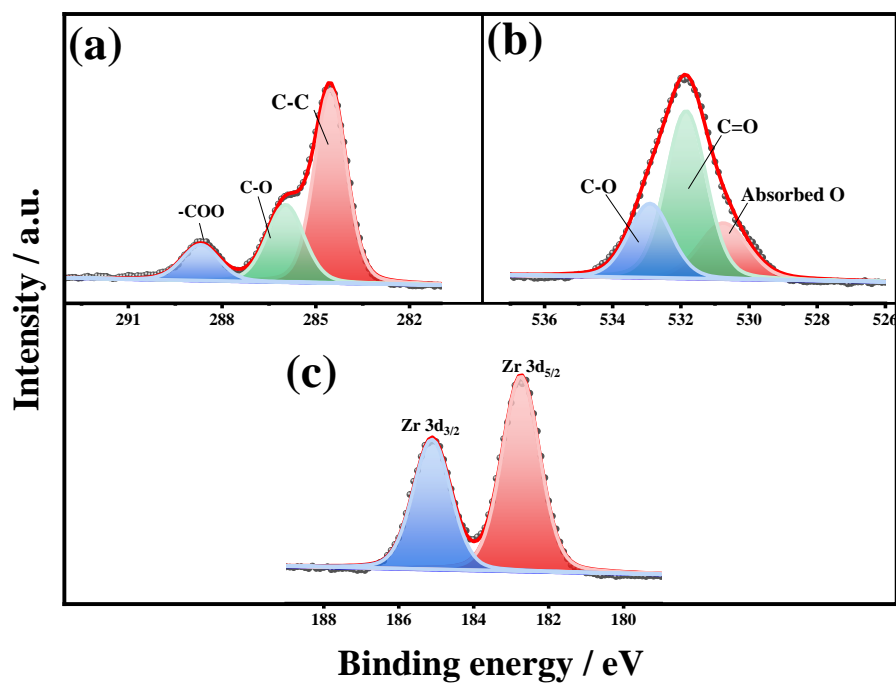
Fig. S9 High-resolution (a) C 1*s*, (b) O 1*s*, and (c) Zr 3*d* XPS spectra of polyUiO-66.

Fig. S10 High-resolution (a) Zr 3*d*, (b) C 1*s*, (c) O 1*s*, and (d) Ag 3*d* XPS spectra of UiO-66@AgNPs.

Fig. S11 High-resolution (a) Zr 3*d*, (b) C 1*s*, (c) N 1*s*, and (d) S 2*p* XPS spectra of Ab/polyUiO-66@AgNPs.

Fig. S12 High-resolution (a) Zr 3*d*, (b) C 1*s*, (c) N 1*s*, and (d) P 2*p* XPS spectra of Apt/polyUiO-66@AgNPs.

Table S1 The porous parameters of UiO-66, UiO-66@AgNPs, polyUiO-66, and polyUiO-66@AgNPs.

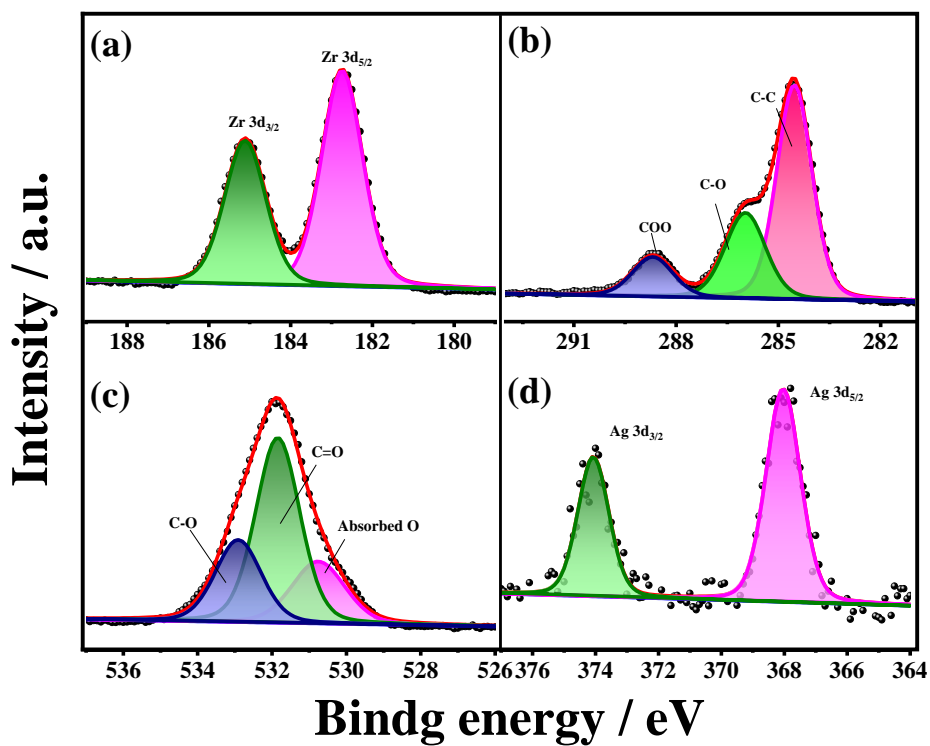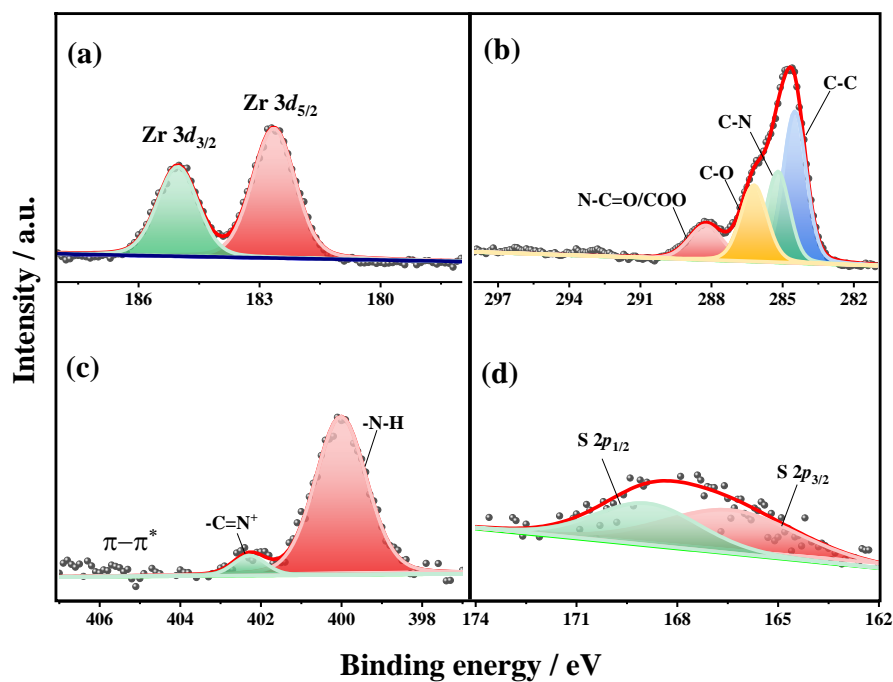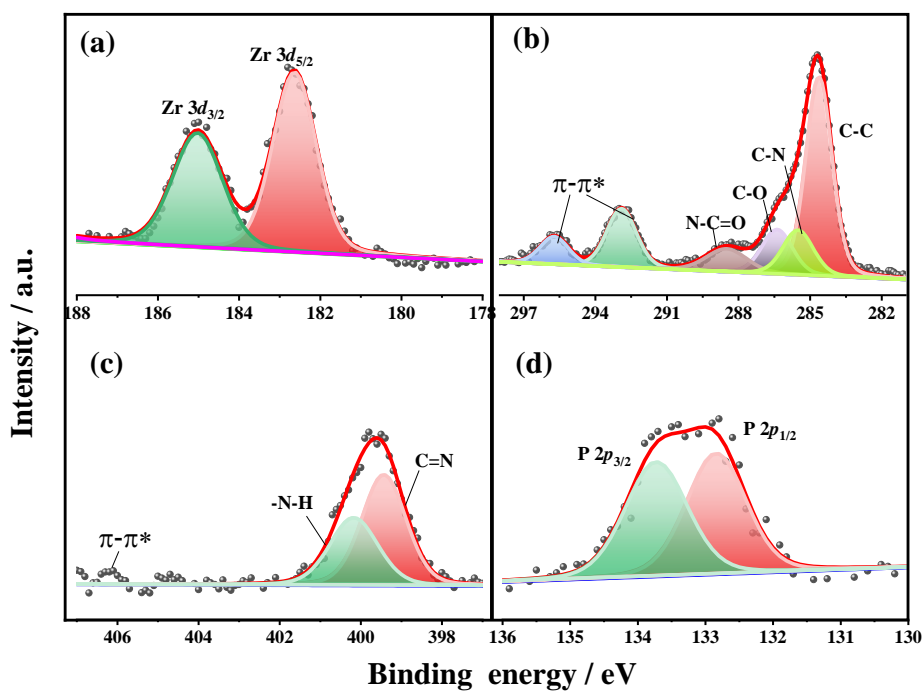| Sample	UiO-66	UiO-66@AgNPs	polyUiO-66	polyUiO-66@AgNPs
BET surface area ($m^2\,g^{-1}$)	1420.9	631.7	604.8	475.0
Mean pore diameter (nm)	1.90	2.10	1.99	2.76
Total Pore volumes ($cm^3\,g^{-1}$)	0.68	0.33	0.23	0.33

Table S2 The element content of UiO-66, UiO-66@AgNPs, polyUiO-66, and polyUiO-66@AgNPs derived from XPS spectra.

Element content (%)	C	O	Zr	Ag
UiO-66	25.53	49.43	22.93	-
polyUiO-66	50.06	36.23	12.57	-
UiO-66@AgNPs	32.55	46.98	17.84	2.63
polyUiO-66@AgNPs	30.87	45.81	15.14	8.18

The morphology of ployUiO-66 shows better dispersion, uniform particles size, and regular spheres than that of UiO-66. BET results reveal that polyUiO-66 possess larger microporous with the pore diameter of 0.56 nm than that of UiO-66 (0.46 nm calculated by the HK method), indicating that the polymer chains could enlarge the pore diameter. Moreover, UiO-66@AgNPs were also prepared using the same method with polyUiO-66@AgNPs. The XPS was also used to determine the chemical composition of the UiO-66@AgNPs (**Fig. S10**). **Table S2** summarizes the element contents in UiO-66@AgNPs and polyUiO-66@AgNPs. UiO-66@AgNPs and polyUiO-66@AgNPs have identical element components. However, polyUiO-66@AgNPs shows higher atom content of Ag

(8.18%), than that of UiO-66@AgNPs (2.63%). It is due to that the non-coordinating polymer chains anchor more Ag atoms, leading to a higher Ag content in the polyUiO-66@AgNPs.

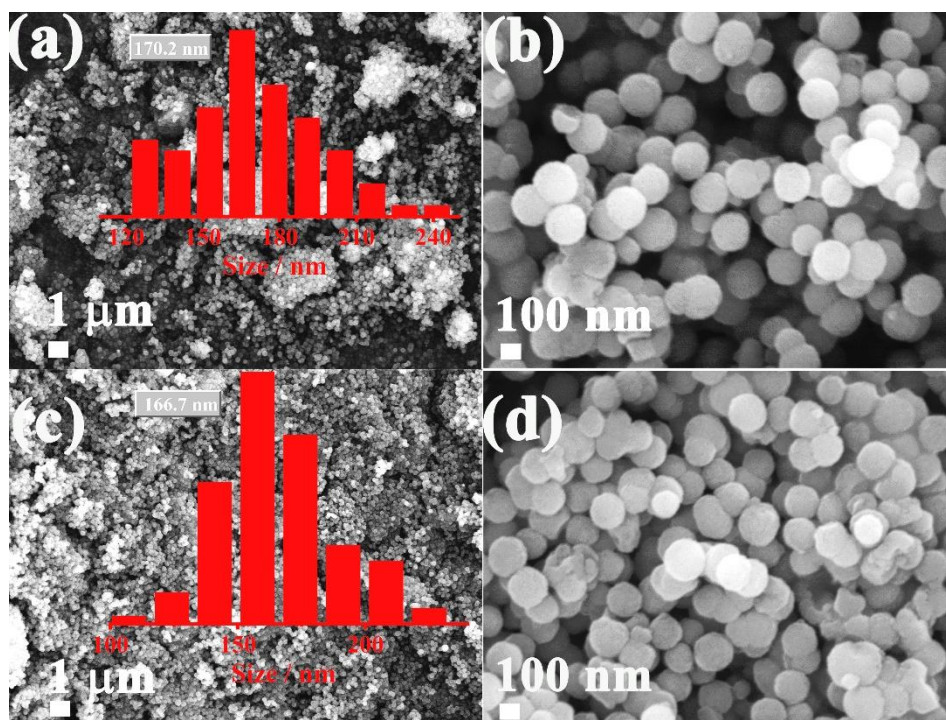## S3. Characterizations of the series of polyUiO-66@AgNPs

Fig. S13 Low- and high-magnification SEM images of (a, b) polyUiO-66@AgNPs$_{6.74}$, and (c, d) polyUiO-66@AgNPs$_{1.33}$.
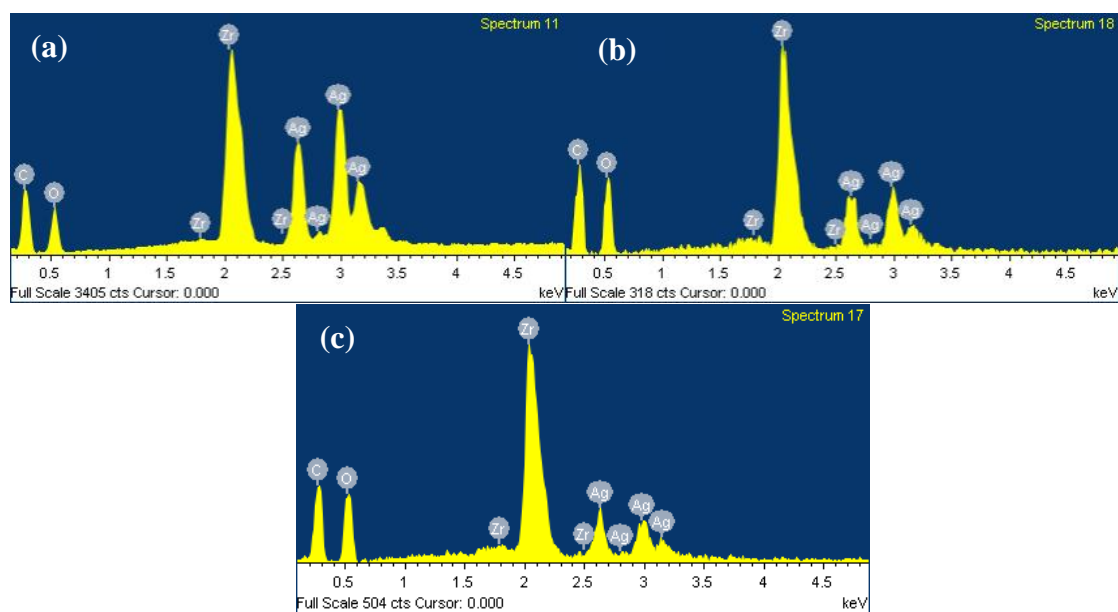

Fig. S14 Energy dispersive spectra (EDS) analysis of (a) polyUiO-66@AgNPs$_{6.74}$, (b) polyUiO-66@AgNPs, and (c) polyUiO-66@AgNPs$_{1.33}$.

Table S3 Element contents calculated from EDS of polyUiO-66@AgNPs.

	C %	O %	Zr %	Ag %
polyUiO-66@AgNPs$_{6.74}$	54.47 ± 1.63	31.41 ± 0.94	7.38 ± 0.22	6.74 ± 0.20
polyUiO-66@AgNPs	56.29 ± 1.69	35.87 ± 1.08	5.79 ± 0.17	2.05 ± 0.06
polyUiO-66@AgNPs$_{1.33}$	58.83 ± 1.76	33.97 ± 1.02	5.87 ± 0.18	1.33 ± 0.04
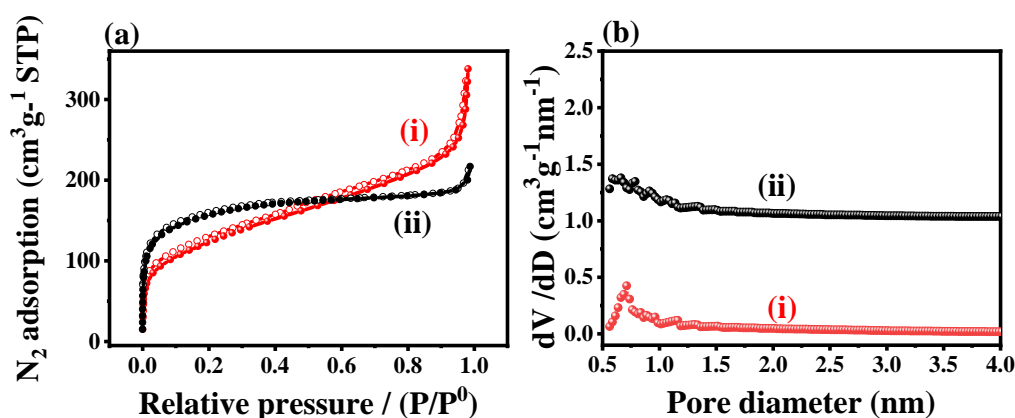
Fig. S15 (a) Nitrogen adsorption-desorption isotherm and (b) HK pore size distribution of (i) polyUiO-66@AgNPs$_{6.74}$ and (ii) polyUiO-66@AgNPs$_{1.33}$.

Characterizations and electrochemical performances of polyUiO-66@AgNPs were shown in **Figs. S13-S15**. The SEM images (**Fig. S13**) of polyUiO-66@AgNPs indicate different AgNPs contents. It is clear that the three polyUiO-66@AgNPs composites are composed of uniform spheres with an average particle size of ca. 166 nm, with particle size distributions ranging from 100 to 250 nm. The contents of AgNPs in polyUiO-66@AgNPs were evaluated by EDS, as indicated in **Fig. S14**. **Table S3** summarizes the percent contents of Zr, Ag, C, and O, in which the Ag content in the series of polyUiO-66@AgNPs are 6.74%, 2.05%, and 1.33%, respectively, which are denoted as polyUiO-66@AgNPs$_{6.74}$, polyUiO-66@AgNPs$_{2.05}$ and polyUiO-66@AgNPs$_{1.33}$. Here, polyUiO-66@AgNPs was used to represent polyUiO-66@AgNPs in the whole manuscript. The N$_2$ adsorption isotherms of polyUiO-66@AgNPs$_{6.74}$ and polyUiO-66@AgNPs$_{1.33}$ (**Fig.**

S15) are assigned to type-II and type-I isotherms, respectively. The BET surface areas of polyUiO-66@AgNPs$_{6.74}$ and polyUiO-66@AgNPs$_{1.33}$ are 396.0 and 559.3 m^2 g^{-1}, respectively. It hints that the BET surface area of composites decreases with increasing the content of AgNPs. The total pore volumes of polyUiO-66@AgNPs$_{6.74}$ and polyUiO-66@AgNPs$_{1.33}$ are 0.5227 and 0.3354 cm^3 g^{-1}, and the mean pore diameters of polyUiO-66@AgNPs$_{6.74}$ and polyUiO-66@AgNPs$_{1.33}$ are 4.86 and 2.40 nm, respectively.

S4. Optimization of experimental conditions for the biosensor

Fig. S16a shows the EIS responses for H1N1 with the polyUiO-66@AgNPs-based biosensor, constructed by coating polyUiO-66@AgNPs suspensions of 0.1, 0.2, 0.5, 1, and 5 mg mL^{-1}. Clearly, the obtained ΔR_{ct} values caused by the determination of H1N1 increases with increasing the suspension concentration from 0.1 to 1 mg mL^{-1}. It reveals that more and more antibody molecules can be adsorbed with increasing the polyUiO-66@AgNPs usage, which results in the recognization of more H1N1 antibodies. When the suspension concentration is large than 1 mg mL^{-1}, no apparent increment in the EIS response is found, hinting both the antibody sorption and specific combination between antibody and H1N1 are up to a platform. As observed in experiments, when the layer is too thick, it will easily detach from the AE surface. Thereby, the polyUiO-66@AgNPs suspension with a concentration of 1 mg mL^{-1} is regarded as the optimal usage for the development of biosensor.

As demonstrated in **Fig. S16b**, the R_{ct} values for antibody adsorption increase with increasing the antibody concentration from 10 to 200 nM, indicating that more antibody molecules could be anchored over the platform at the large concentrations. It thus leads to the formation of antibody-antigen complexes. However, if the antibody concentration is large than 100 nM, the R_{ct} values for anchoring antibody are up to equilibrium, which reveals the saturation for antibody adsorption. Thus, the optimal antibody concentration is set as 100 nM for the construction of biosensor.

The effect of incubation time on the sensing performances was also evaluated. The diameter of semicircle comprising in EIS Nyquist plots (**Fig. S16c**), which are obtained for detection of H1N1 and recorded at different durations, increases with the incubation time going on. This reveals that more H1N1 is combined with antibody, thus improving the EIS response. After 30 min, the obtained EIS response does not increases any more, indicating the combination of antibody and antigen achieves a balance. The deduced R_{ct} values (**Fig. S16d**) also obey this trend, meaning that the duration of 30 min for binding antigen is optimal for detection of H1N1.

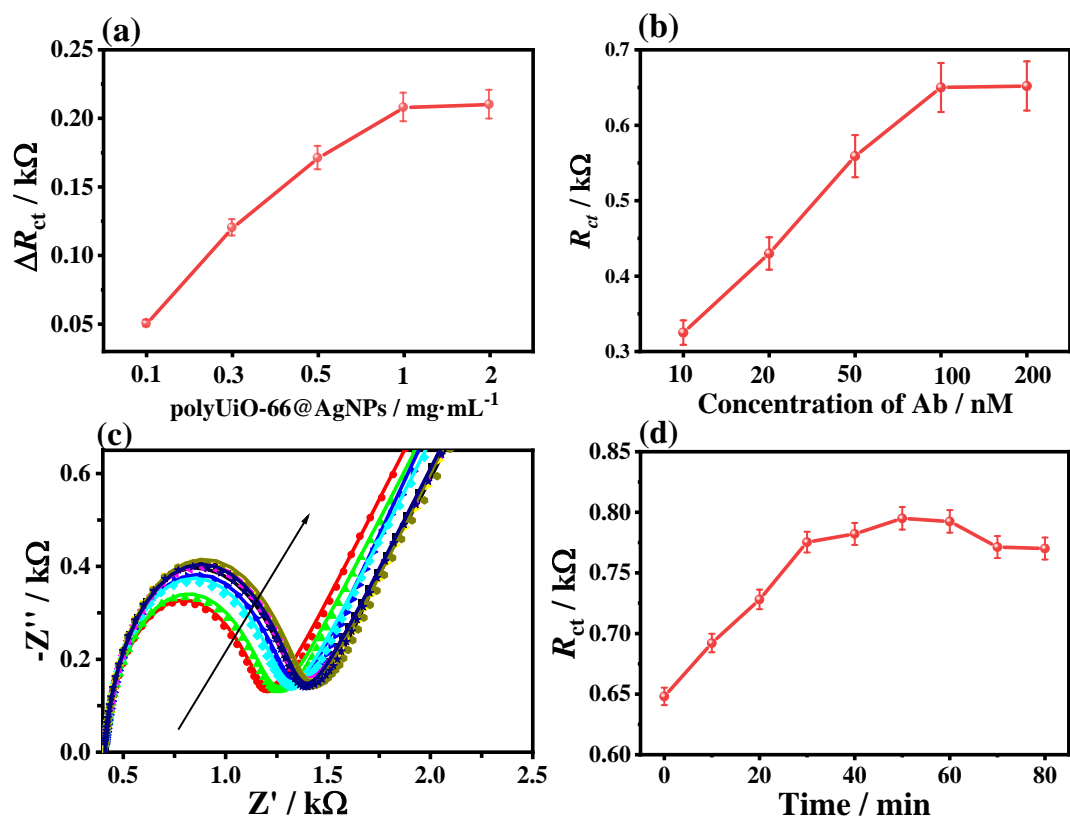**Fig. S16** (a) Variation in charge-transfer resistance (ΔR_{ct}) for H1N1 detection using the biosensor with polyUiO-66@AgNPs concentrations of 0.1, 0.2, 0.5, 1.0, and 2.0 mg mL^{-1}. (b) The influence of antibody concentrations on H1N1 detection. (c) EIS Nyquist plots of polyUiO-66@AgNPs-based biosensor incubated with H1N1 solution (0.1 pg mL^{-1}) for different durations and (d) the corresponding R_{ct} values.

S5. Electrochemical sensing performances for influenza A (H1N1)
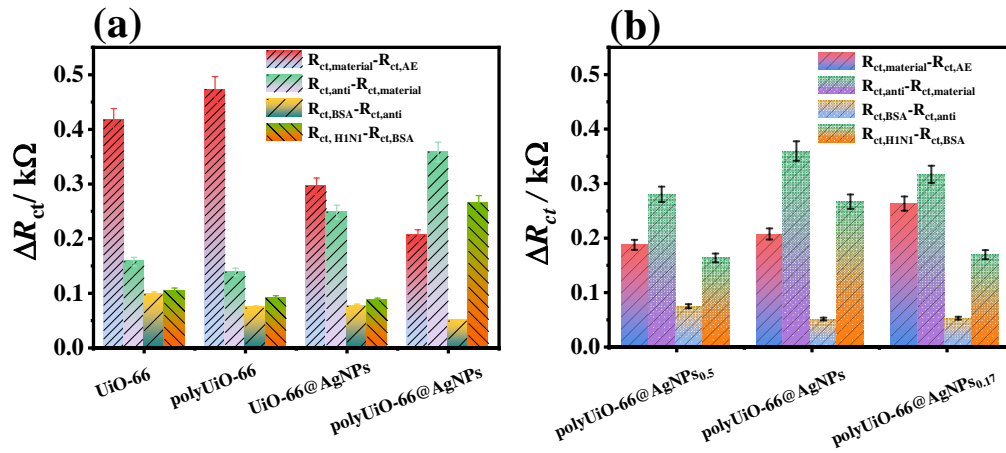
Fig. S17 (a) ΔR_{ct} values of the immunosensors based on UiO-66, polyUiO-66, UiO-66@AgNPs, and polyUiO-66@AgNPs, and **(b)** ΔR_{ct} values of the immunosensors based on polyUiO-66@AgNPs$_{6.74}$, polyUiO-66@AgNPs, and polyUiO-66@AgNPs$_{1.33}$ for the detection of H1N1.

Fig. S18 EIS Nyquist plots for the construction of immunosensors based on (a) UiO-66, (b) polyUiO-66, (c) UiO-66@AgNPs, (d) polyUiO-66@AgNPs$_{6.74}$, and (e) polyUiO-66@AgNPs$_{1.33}$ for the detection of H1N1.

Fig. S19 DPV curves of for the construction of immunosensors based on (a) UiO-66, (b) polyUiO-66, (c) UiO-66@AgNPs, (d) polyUiO-66@AgNPs$_{6.74}$, and (e) polyUiO-66@AgNPs$_{1.33}$ for the detection of H1N1.

Fig. S20 CV curves of AEs modified using (a) UiO-66, (b) polyUiO-66, (c) UiO-66@AgNPs, (d) polyUiO-66@AgNPs$_{6.74}$, (e) polyUiO-66@AgNPs, and (f) polyUiO-66@AgNPs$_{1.33}$ for detecting H1N1.
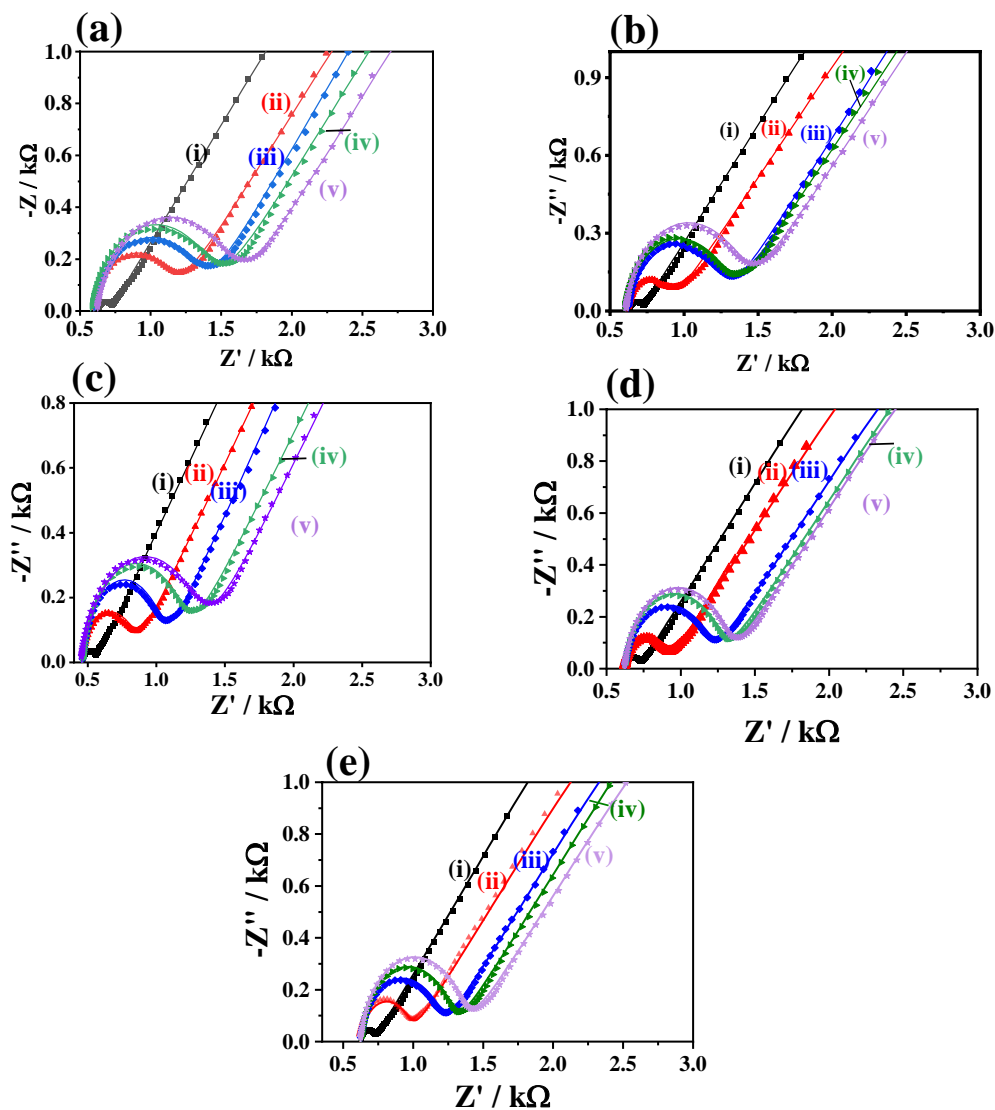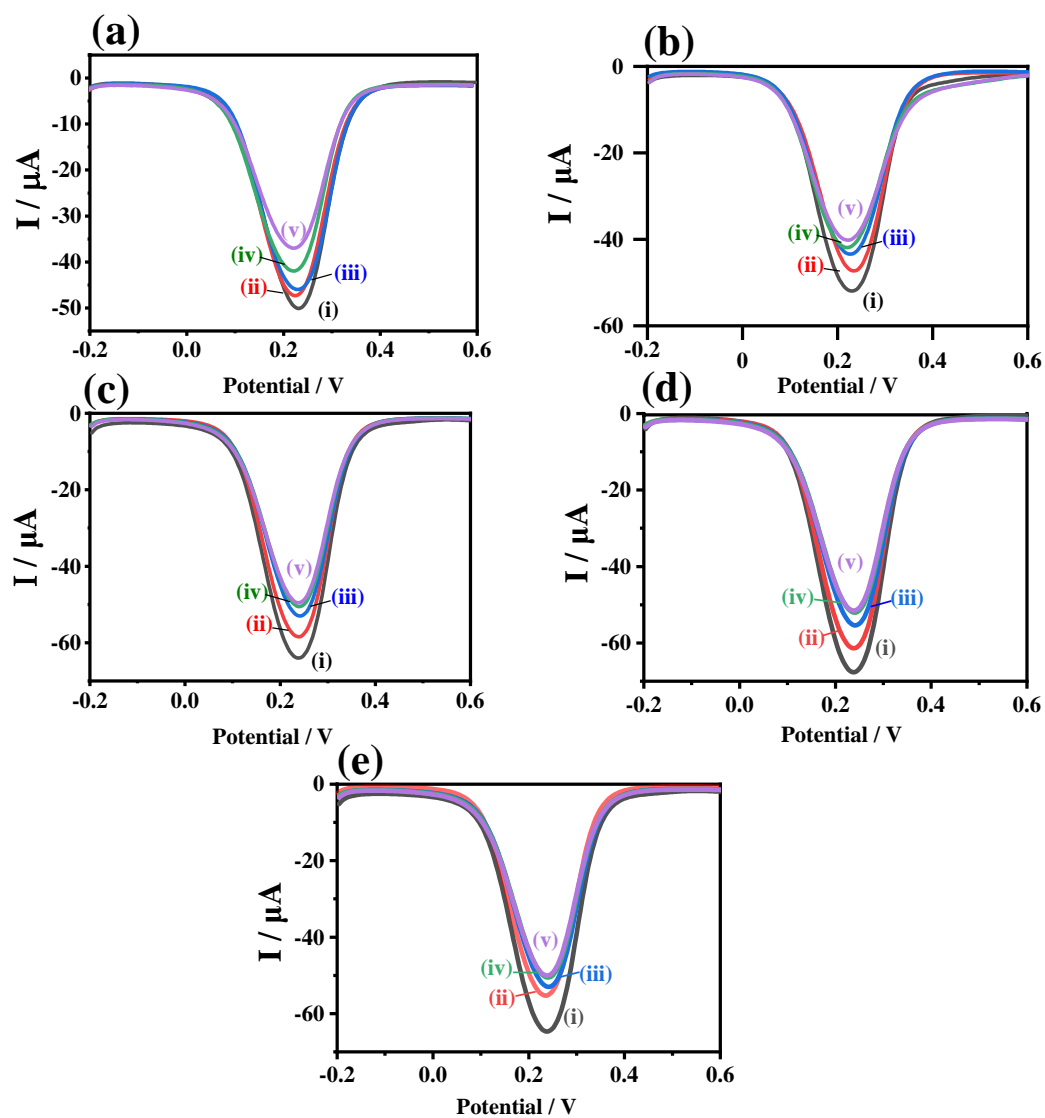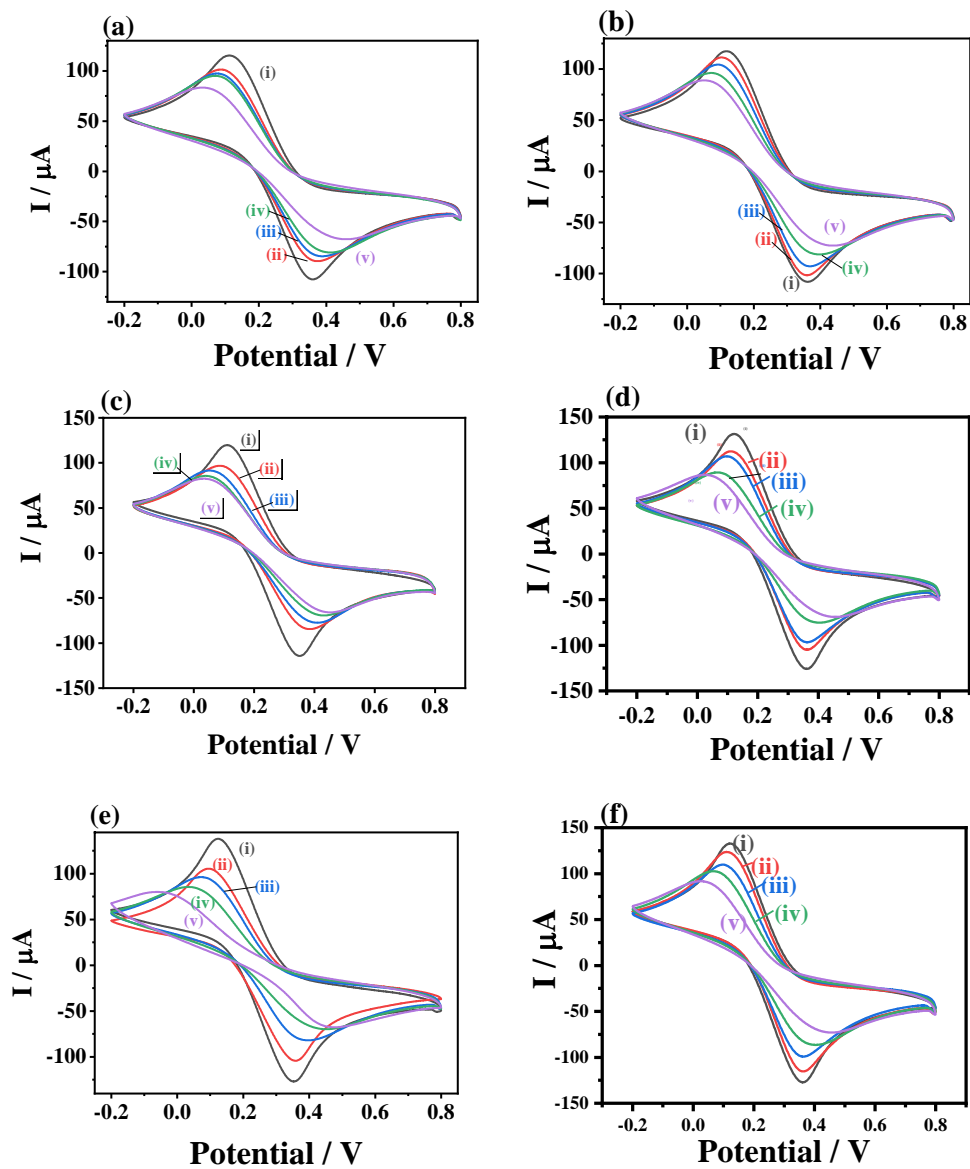
Table S4 R_{ct} values of the biosensors based on UiO-66, polyUiO-66, UiO-66@AgNPs, polyUiO-66@AgNPs$_{6.74}$, polyUiO-66@AgNPs, and polyUiO-66@AgNPs$_{1.33}$ for detection of H1N1.

Electrode materials	R_{ct} (Ω)					θ (%)
	Bare AE	Modified Electrode	Immobilization of antibody	Adsorbed BSA	Detection of H1N1	
UiO-66	83	500	658	755.6	860	24.01
polyUiO-66	80	553	692	765.2	856.3	20.09
UiO-66@AgNPs	84	380	628.6	705	792	39.55
polyUiO-66@AgNPs$_{6.74}$	85	271	550	623	785	50.73
polyUiO-66@AgNPs	84	290	648.6	698	963.5	55.29
polyUiO-66@AgNPs$_{1.33}$	83	345	661	712	880	47.81

Table S5 I values of the biosensors based on UiO-66, polyUiO-66, UiO-66@AgNPs, polyUiO-66@AgNPs$_{6.74}$, polyUiO-66@AgNPs, and polyUiO-66@AgNPs$_{1.33}$ for detection of H1N1.

Electrode materials	I (μA)				
	Bare AE	Modified Electrode	Immobilization of antibody	Adsorbed BSA	Detection of H1N1
UiO-66	50.12	47.31	45.96	41.94	37.01
polyUiO-66	64.02	58.45	53.01	50.54	49.53
UiO-66@AgNPs	51.95	47.31	43.43	41.91	40.18
polyUiO-66@AgNPs$_{6.74}$	67.62	61.37	55.37	52.05	51.53
polyUiO-66@AgNPs	50.93	45.63	44.45	40.25	39.07
polyUiO-66@AgNPs$_{1.33}$	64.66	56.14	53.01	50.54	50.02

As shown in **Figs. S17-20** and **Table S4-S5**, UiO-66 and UiO-66@AgNPs were also used to construct biosensor to detect H1N1 for comparison with polyUiO-66 and polyUiO-66@AgNPs. The polyUiO-66@AgNPs-based biosensor exhibits the higher electrochemical activity and detection amount of H1N1 than that of the UiO-66-, UiO-66@AgNPs, or polyUiO-66-based biosensor. Moreover, both polyUiO-66@AgNPs$_{6.74}$ and polyUiO-66@AgNPs$_{1.33}$ were utilized to construct the H1N1 immunosensor, for which the detection procedures were assessed. All biosensors show a similar tendency for constructing procedure with polyUiO-66@AgNPs-based immunosensor, indicating that the appropriate AgNPs content in polyUiO-66@AgNPs can improve the sensitivity of the fabricated biosensors. Thereby, the polyUiO-66@AgNPs was selected as sensing material to construct the biosensor for detection of H1N1 and N-gene of SARS-CoV2.

Fig. S21 (a) Selectivity, (b) reproducibility, (c) stability, and (d) regenerability of the polyUiO-66@AgNPs-based sensor for detection of 0.1 pg mL^{-1} (H1N1) using DPV. The error bars represent the average standard errors for three measurements (n = 3).

S6. Electrochemical sensing performances for N-gene of SARS-CoV-2
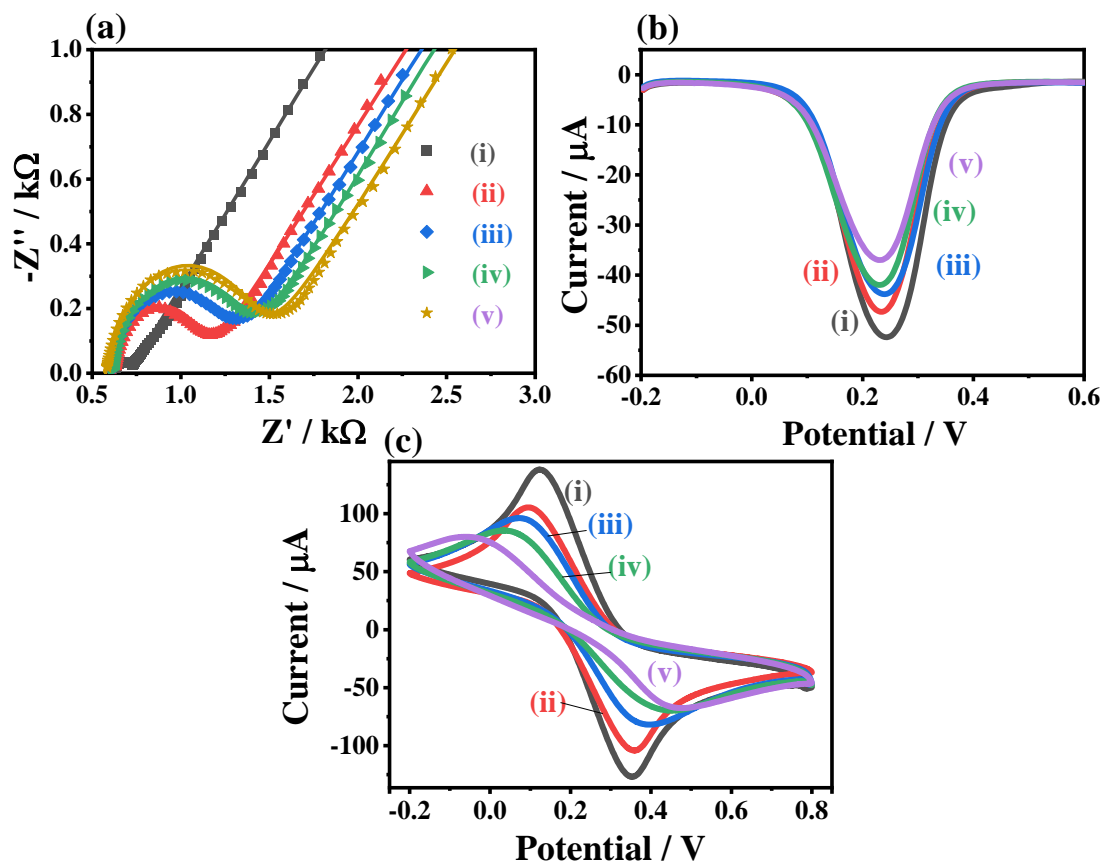
Fig. S22 (a) EIS Nyquist plots, (b) DPV curves, and (c) CV curves of the polyUiO-66@AgNPs-based biosensor for detecting SARS-CoV2 N-gene in 0.1 M PBS containing 5 mM $[Fe(CN)_6]^{3-/4-}$, including (i) AE, (ii) polyUiO-66@AgNPs/AE, (iii) Apt/polyUiO-66@AgNPs/AE, (iv) BSA/Apt/polyUiO-66@AgNPs/AE, and (v) SARS-CoV2 N-gene/BSA/Apt/polyUiO-66@AgNPs/AE.
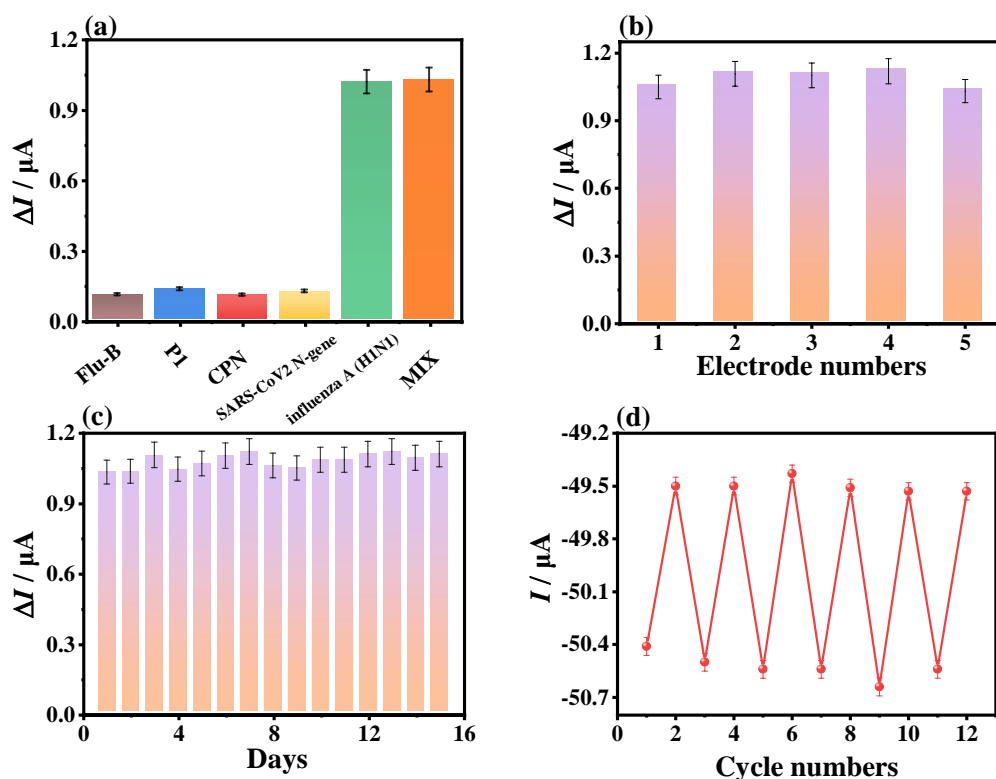
Fig. S23 (a) Selectivity, (b) reproducibility, (c) stability, and (d) regenerability of the polyUiO-66@AgNPs-based sensor for the detection of 0.1 pg mL^{-1} SARS-CoV2 N-gene by DPV. The error bars represent average standard errors for three measurements (n = 3).
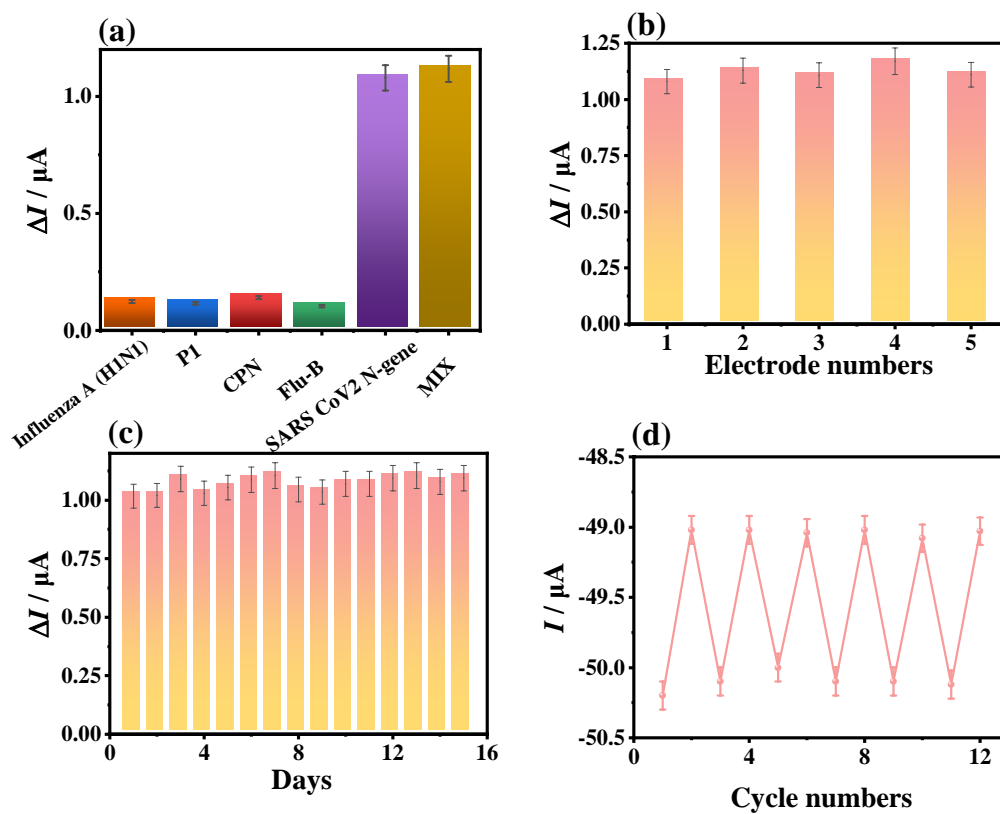
Table S6 The sensitive performances of the biosensors based on polyUiO-66@AgNPs for detection influenza A (H1N1) and SARS-CoV2 N-gene using EIS and DPV methods.

Targets	EIS				DPV			
	Regression equation	LOD (fg·mL^{-1})	Linear range (fg·mL^{-1})	R^2	Regression equation	LOD (fg·mL^{-1})	Linear range (fg·mL^{-1})	R^2
Influenza A (H1N1)	ΔR_{ct} (kΩ) = 0.23 logC$_{H1N1}$ (pg mL^{-1}) + 0.35	54.7	100-1×10^9	0.9982	ΔR_{ct} (kΩ) = 0.35 log C$_{SARS\text{-}CoV2\ gene}$ (pg mL^{-1}) + 0.39	49.4	100-1×10^9	0.9921
SARS-CoV2 N-gene	ΔI (μA) = 4.81 logC$_{H1N1}$ (pg mL^{-1}) + 6.37	23.4	100-1×10^6	0.9932	ΔI (μA) = 7.65 log C$_{SARS\text{-}CoV2\ gene}$ (pg mL^{-1}) + 8.72	18.2	100-1×10^6	0.9982

S7. Application analysis of the biosensors

Table S7 Determination of H1N1 in human serum by the proposed biosensor (n = 3).

Added amount (pg mL^{-1})	Found amount (pg mL^{-1})	Apparent recovery (%)	RSD (%)
0.1	0.099	99.00	1.53
1	1.00	100.30	1.42
10	0.99	99.50	1.12
10^2	100.20	100.20	1.31
10^3	998.20	99.82	1.23
10^4	9895.40	98.95	1.62
10^5	100000.60	100.00	1.54
10^6	1000023.50	100.00	0.95

Table S8 Determination of SARS-CoV2 N-gene in human serum by the proposed aptasensor (n = 3).

Added amount (pg mL^{-1})	Found amount (pg mL^{-1})	Apparent recovery (%)	RSD (%)
0.1	0.098	98.00	1.23
1	0.99	99.70	0.92
5	5.02	100.40	1.11
10	10.03	100.30	1.41
50	49.88	99.76	1.19
100	100.20	100.20	1.52
1000	987.60	98.76	1.59

Table S9 Determination of SARS-CoV2 N-gene in human saliva by the proposed aptasensor (n = 3).

Added amount (pg mL^{-1})	Found amount (pg mL^{-1})	Apparent recovery (%)	RSD (%)
0.1	0.095	95.00	1.53
1	1.02	102.70	1.68
5	5.10	102.00	2.11
10	10.13	101.30	1.31
50	48.78	97.56	1.39
100	101.40	101.40	1.52
1000	982.40	98.24	1.35

Table S10 Determination of SARS-CoV2 N-gene in frozen shrimp by the proposed aptasensor (n = 3).

Added amount (pg mL^{-1})	Found amount (pg mL^{-1})	Apparent recovery (%)	RSD (%)
0.1	0.11	108.00	1.43
1	1.01	101.00	1.68
5	4.95	99.00	1.81
10	10.08	100.80	1.51
50	49.10	98.20	1.19
100	101.60	101.60	1.72
1000	977.40	97.74	2.15